

Active topoelectrical circuits

Tejas Kotwal,^{1,2} Henrik Ronellenfitsch,² Fischer Moseley,³ and Jörn Dunkel²

¹*Department of Mathematics, Indian Institute of Technology Bombay, Mumbai 400076, India*

²*Department of Mathematics, Massachusetts Institute of Technology,
77 Massachusetts Avenue, Cambridge, MA 02139, U.S.A.*

³*Department of Physics, Massachusetts Institute of Technology,
77 Massachusetts Avenue, Cambridge, MA 02139, U.S.A.*

(Dated: May 17, 2022)

We develop design principles for active topoelectrical circuits (ATCs) by exploiting a mathematical correspondence between active mechanical metamaterials and nonlinear electronic circuits. Building on a generic nonlinear oscillator representation of active circuit elements, we demonstrate and characterize self-organized, self-sustained, topologically protected, global edge states for both one-dimensional (1D) and two-dimensional (2D) ATCs. Furthermore, our analysis shows how one can induce persistent localized bulk wave patterns by strategically placing defects in 2D lattice ATCs. These results provide key elements for the practical realization of autonomous electrical circuits with robust functionality in arbitrarily high dimensions.

Information transfer and storage in natural and man-made active systems, from sensory organs [1–3] to the internet, rely on the robust exchange of electrical signals between a large number of autonomous units that balance local energy uptake and dissipation [4, 5]. Recent advances in the understanding of photonic [6–8], acoustic [9] and mechanical [10–13] metamaterials have shown that topological protection [14–19] enables the stabilization and localization of signal propagation in passive and active [20, 21] dynamical systems that violate time-reversal and/or other symmetries. Important recent work has successfully applied these ideas to realize passive, linear [22–26] and nonlinear [27–29] topoelectrical circuits that exhibit decaying topologically protected modes. Despite substantial recent progress in the development of topological nonlinear optics [30–34] and transmission lines [35–38], the generalization to active [39, 40] nonlinear circuits consisting of autonomously acting units [41] still poses theoretical and practical challenges. Exploiting a mathematical analogy with active Brownian particle systems [21], we develop and demonstrate general design principles for active topoelectrical circuits (ATCs) that achieve self-organized, self-sustained, topologically protected current patterns. The main building blocks of ATCs are nonlinear dissipative elements that exhibit an effectively negative resistance (NR) over a certain voltage range. NRs can be realized using van der Pol (vdP) circuits [42], tunnel diodes, unijunction transistors or solid-state thyristors [43], and the design principles described below are applicable to all these systems.

Active electronic circuits have been studied previously as models of neuronal networks [42] and solitary signal transport [4, 5]. To leading order, the NR elements in an active circuit can be described [4, 5] by a Rayleigh-type resistance $R(V) = -(\alpha - 3\gamma V^2)$, where α and γ are positive parameters. An archetypal example is the vdP oscillator circuit with capacitance C and inductance L_{ii} , as shown in Fig. 1(a). When expressed in terms of the

rescaled dimensionless voltage $\hat{V}_i = x_i = \sqrt{3\gamma/\alpha} V_i$, the dynamics of an isolated vdP-unit i is governed by [44]

$$\ddot{x}_i - \varepsilon(1 - x_i^2)\dot{x}_i + x_i = 0. \quad (1)$$

where $\varepsilon = \alpha\sqrt{L/C}$, $t = \sqrt{LC}\hat{t}$, and $\dot{x}_i = dx_i/d\hat{t}$. Equation (1) is intimately related to that of a harmonically trapped active Brownian particle [45], with position coordinate y and velocity $u = \dot{y}$ described by the standard cubic friction model $\dot{u} = \varepsilon(1 - u^2/3)u - y$. Upon taking the time derivative and identifying $u = \dot{y} = x_i$, one recovers Eq. (1). It was shown recently [21] that suitably coupled mechanical chains of active Brownian particles can autonomously actuate topological modes. This insight can be used as guidance for the design of ATCs.

To design an ATC with desired topological properties, we generalize Eq. (1) by introducing suitably chosen couplings between vdP units i and j through inductances L_{ij} ; see Fig. 1(b,c) for two examples. Assuming a lattice of vdP units and introducing the symmetric coupling matrix elements $\beta_{ij} = -L_0/L_{ij}$ for $i \neq j$, and $\beta_{ii} = L_0(1/L_{ii} + \sum_{k \neq i} 1/L_{ik})$, Eq. (1) generalizes to

$$\ddot{x}_i - \varepsilon(1 - x_i^2)\dot{x}_i + \sum_j \beta_{ij}x_j = 0, \quad (2)$$

where L_0 is the smallest inductance in the circuit (Supplementary Information).

Interpreting each individual vdP unit as a vertex node in the network graph [Fig. 1(b,c)], the effective dimension d of the ATC can be tuned by increasing the number of couplings; in principle, arbitrary values $d \geq 1$ are realizable with densely connected large networks. For example, for d -dimensional cubic lattices, rows of the coupling matrix $\beta = (\beta_{ij})$ corresponding to bulk nodes will have $2d$ off-diagonal entries. Below, we will focus on the cases $d = 1$ [Fig. 1(b)] and $d = 2$ [Fig. 1(c)] to demonstrate the implementation and key properties of ATCs. Generally, through an appropriate choice of β , it is possible to realize a wide range of topological phases.

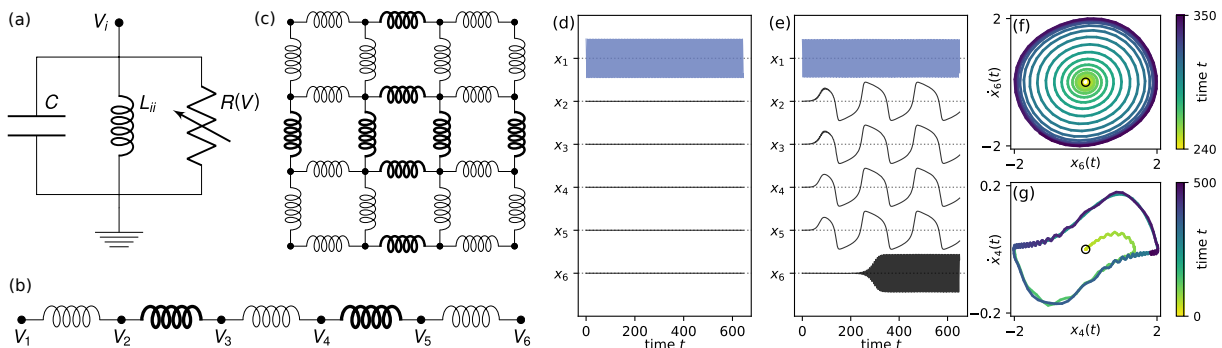


FIG. 1. Schematic and dynamics of active topoelectrical SSH circuits. (a) Circuit diagram of a basic vdP oscillator with capacitance C , inductance L_{ii} and nonlinear resistor $R(V)$. (b,c) 1D and 2D SSH circuits where each node is a vdP oscillator. Thick lines indicate strong coupling s and thin lines weak coupling $w \ll s$. (d) Oscillator dynamics in an undamped passive ($\varepsilon = 0$) 1D SSH circuit with 6 nodes. Applying a nonzero initial voltage at the first node, the oscillation remains exponentially localized on that edge. (e–g) Dynamics of a 1D ATC ($\varepsilon > 0$) for the same initial condition as in (d). (e) The high-frequency topological edge mode is activated first and induces slow synchronized bulk oscillations, which eventually actuate the second topological mode at the opposite end. Phase portraits of the boundary (f) and bulk (g) nodes show the limit cycles of the fast and slow oscillations. The edge oscillators show approximately circular limit cycles typical of weak nonlinearity while the bulk dynamics is of strong relaxation type despite ε being small. Simulation parameters in (d–e): $g = 1$, $w = 0.003$, $s = g - w$ with $\varepsilon = 0$ in (d) and $\varepsilon = 0.1$ in (e–g). Initial conditions: $x_1(0) = 2$ and $\dot{x}_1(0) = \dot{x}_j(0) = \dot{x}_j(0) = 0$ for $j \geq 2$.

As a first realization of an ATC, we consider the coupling matrix of a one-dimensional (1D) Su-Schrieffer-Heeger (SSH) model. Originally introduced to describe spinless fermions [46], the SSH model is known to support topologically protected boundary modes in a variety of quantum [47] and classical [13, 21, 23] systems. The $n \times n$ SSH coupling matrix for the case of $n = 6$ unit vdPs reads

$$\beta = \begin{pmatrix} g & -w & 0 & 0 & 0 & 0 \\ -w & g & -s & 0 & 0 & 0 \\ 0 & -s & g & -w & 0 & 0 \\ 0 & 0 & -w & g & -s & 0 \\ 0 & 0 & 0 & -s & g & -w \\ 0 & 0 & 0 & 0 & -w & g \end{pmatrix}, \quad (3)$$

with the diagonal elements $\beta_{ii} = g > 0$ representing the electrical grounds. In our electrical circuits, ground inductances L_{ii} are chosen such that $g = L_0(1/L_{ii} + \sum_{k \neq i} 1/L_{ik})$ for all i . The off-diagonal entries $w > 0$ and $s > w > 0$ encode the weak and strong couplings, respectively (Supplementary Information). Adding more units extends the matrix symmetrically along the diagonal. The strongly coupled nodes form ‘dimers’ which are connected to each other through weak bonds [thin lines in Fig. 1(b)].

To gain intuition about the dynamics of the 1D SSH circuit, it is instructive to first consider the passive topoelectrical SSH circuit with $\varepsilon = 0$ and $s \gg w$. Then, Eqs. (2) and (3) reduce to a linear dynamical system that exhibits topologically protected, exponentially localized modes at both ends of the chain [47]. These edge modes have finite-frequency for $g > 0$ and become zero-modes

as $g \rightarrow 0$. Their presence can be illustrated by considering a passive circuit in the almost fully dimerized topological regime ($w \ll s$) with all nodes initially at rest, $x_i(t) = \dot{x}_i(t) = 0$ for $t < 0$. Upon initializing the chain by imposing a nonzero voltage value at the left edge, $x_1(0) > 0$, the boundary node will oscillate with a nonzero amplitude at frequency \sqrt{g} , while the amplitudes of the other nodes remain exponentially small [Fig. 1(d)]. In the next part, we will see that ATCs with $\varepsilon > 0$ exhibit fundamentally different behaviors that promise a broad range of novel applications.

Adding just a small amount of activity ($0 < \varepsilon \ll \sqrt{g}$) significantly alters the dynamics of the edge and bulk oscillators [Fig. 1(e–g)]. In the topological regime, characterized by $s \gg w$ and $g \geq s + w$, the boundary nodes are only weakly coupled to the bulk and behave similarly to isolated vdP oscillators. The active local energy input renders the rest state ($x_i = \dot{x}_i = 0$) unstable, forcing the boundary nodes to approach a stable limit cycle corresponding to a fast oscillation at frequency \sqrt{g} [Fig. 1(e,f)]. By contrast, bulk nodes are strongly coupled to one or more neighbors, resulting in a distinctly different bulk dynamics reminiscent of highly nonlinear relaxation oscillations [Fig. 1(e,g)]. For fully decoupled pairs of vdP oscillators, one expects stable phase-locked solutions with relative phase 0 or π [48, 49]. To obtain further analytical insight into the bulk dynamics, we linearize Eqs. (2) near the rest state. The resulting dynamical matrix has eigenvalues $\lambda_{k,\pm} = \frac{1}{2}(\varepsilon \pm \sqrt{\varepsilon^2 - 4\mu_k}) = \pm\sqrt{-\mu_k} + \mathcal{O}(\varepsilon)$, where μ_k are the eigenvalues of the coupling matrix β (Supplementary Information). In the fully dimerized limit ($w \rightarrow 0$), μ_k can be calculated explicitly and one finds two degen-

erate eigenstates at $\mu_k = g$, corresponding to the topologically protected edge modes, and $n - 2$ degenerate bulk modes at $\mu_k = g \pm s$ (Supplementary Information). The bulk eigenvectors are pairwise localized with components $(1, \pm 1)$ on one of the dimers, and zero everywhere else, corresponding to a low-energy in-phase oscillation ($\mu_k = g - s$) and a high-energy anti-phase ($\mu_k = g + s$) oscillation (Supplementary Information). This implies that the dimers' dynamics near the rest state is approximately decoupled and governed by the eigenvalues $\sqrt{-g \mp s}$. If $g > s$, all modes are oscillatory (for $g < s$, the anti-phase mode becomes unstable and may cause damage to the circuit). Armed with these analytical insights, we next characterize numerically the striking nonlinear effects that arise in ATCs. In the simulations, we can fix $g = 1$ without loss of generality, which is equivalent to dividing Eq. (2) by g and rescaling $t \rightarrow t/\sqrt{g}$, $\varepsilon \rightarrow \varepsilon/\sqrt{g}$, $s \rightarrow s/g$ and $w \rightarrow w/g$.

In contrast to passive ($\varepsilon = 0$) topoelectrical circuits, which remain quiescent in the bulk when initiated at the edge [Fig. 1(d)], ATCs with $\varepsilon > 0$ exhibit complex self-organization and synchronization phenomena. To explain the underlying physical mechanisms, we consider the 1D SSH ATC from Fig. 1(b) with the same initial condition as for the passive circuit in Fig. 1(d). When one edge node of the ATC is initialized at time $t = 0$, it rapidly settles into a fast limit-cycle oscillation [Fig. 1(e,f)], as predicted above. As it gets activated, the edge mode imparts a weak external forcing on the neighboring strongly-coupled dimer. The combination of forcing and local energy input from the negative resistance drives the dimer into its low-energy state, characterized by a slow nonlinear in-phase oscillation of the dimer nodes with period $2\pi/\sqrt{g-s}$ [Fig. 1(e,g)]. The first bulk dimer then in turn activates the second dimer, and so on, resulting in a globally synchronized bulk state. The activation front eventually reaches the last node, where it triggers the second topological edge mode [Fig. 1(f)]. The final state of the chain is a robust attractor that is self-sustained and could be used for active solitary signal transmission.

In practice, ATCs can be actuated with a wide range of initial conditions that can lead to different types of stable asymptotic behaviors [Fig. 2]. To investigate the likelihood and characteristics of possible attractors, we simulated the active SSH circuit with $n = 6$ nodes with non-zero initial conditions on the bulk. Since the edge node initial conditions become negligible in this case due to the weak edge-bulk coupling, we fixed zero-initial conditions at the edges. Thus, the topological edge modes are actuated by the bulk dynamics in these simulations. Examples of low-energy and high-energy attractors with slow and fast bulk dimer oscillations, obtained with binary initial conditions in the bulk, $x_i(0) = \pm 0.1$ and $\dot{x}_i(0) = 0$, are shown [Fig. 2(a)]. These attractors can be classified in terms of the relative signs of the $n_b = n - 2 = 4$ bulk

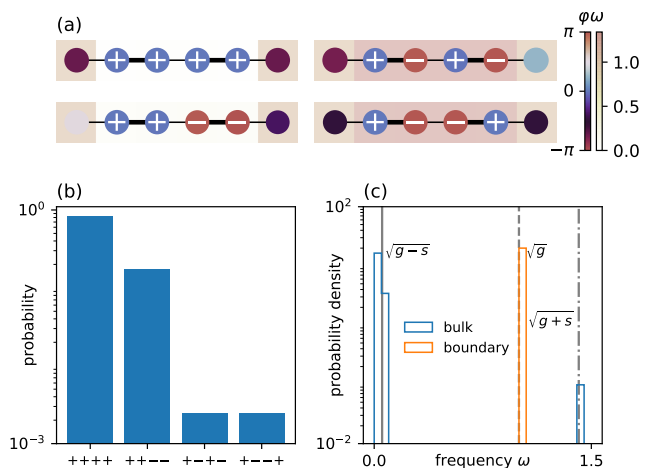


FIG. 2. Attractor statistics of a 1D ATC. (a) An active SSH circuit with $n = 6$ vdP nodes has four qualitatively distinct stable attractors. Circle size represents instantaneous absolute voltage $|x_i(t)|$, symbol color the phase φ and background color the time-averaged frequency $\omega = \langle \dot{\varphi} \rangle$ of the oscillators. Two low-energy attractors exhibit in-phase dynamics of the bulk dimer nodes, and two high-energy attractors show anti-phase dynamics on the bulk dimers. (b) Low-energy attractors are substantially more frequently realized when bulk nodes are initialized with uniformly random $x_i(0) \in [-4, 4]$ and $\dot{x}_i(0) \in [-0.4, 0.4]$. The two in-phase states are approached for $\approx 99.5\%$ of initial conditions. (c) Frequencies of nonlinear bulk oscillations cluster around $\sqrt{g \pm s}$ (solid/dash-dotted line), boundary oscillations around \sqrt{g} (dashed line), as predicted by linearized theory. Simulation parameters: $g = 1, w = 0.003, s = g - w$, and $\varepsilon = 0.1$. Histograms were computed from 50,000 trajectories, integrated up to $t = 1000$.

voltages x_i at a fixed time. Normalizing by the sign of first bulk oscillator, we numerically find that there exist four different stable attractors corresponding to different possible combinations of in-phase and anti-phase dimer oscillations [Fig. 2(a)].

To estimate the likelihood of observing a specific attractor in experiments, we performed 50,000 simulations with randomly chosen bulk initial data. To explore a large neighborhood of the bulk limit cycle [Fig. 1(g)], initial conditions were sampled uniformly from the 8-dimensional domain $x_i(0) \in [-4, 4]$, $\dot{x}_i(0) \in [-0.4, 0.4]$. These simulations predict that, in practice, low-energy states with in-phase bulk dimers are much more likely than high-energy attractors with many anti-phase dimers [Fig. 2(b)]. Mixed in-phase/anti-phase dimer attractors are not observed for this parameter regime. Furthermore, even though the shape of the bulk limit cycles indicate a highly nonlinear relaxation dynamics [Fig. 1(g)], the numerically determined time-averaged frequencies $\langle \dot{\varphi} \rangle$, where $\varphi(t) = \arctan(\dot{x}(t)/x(t))$, agree remarkably well with the bulk oscillation frequencies $\sqrt{g \pm s}$ and boundary oscillation frequency \sqrt{g} predicted

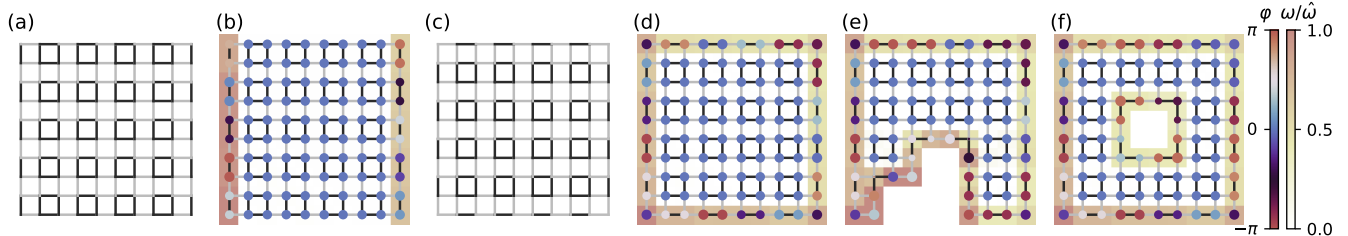


FIG. 3. Self-organized self-sustained nonlinear oscillations recapitulate topological boundary phenomena. (a) Connectivity of the 2D SSH grid in the topological T1-edge mode regime. Thick and thin lines indicate strong and weak couplings, respectively. (b) Snapshot of the vdP network dynamics on the grid (a), with nodes colored by the phase angle φ in the (x_i, \dot{x}_i) plane; background color shows time averaged node frequency $\omega = \langle \dot{\varphi} \rangle$ normalized by the maximum $\hat{\omega}$ over all oscillators. Even though the initial voltage was non-zero only on the bottom left corner node, the circuit autonomously actuates two topological edge oscillations with mean frequency $\hat{\omega}$, while the bulk synchronizes in-phase. (c) Connectivity of the 2D SSH grid in the topological T2-corner mode regime. (d) Snapshot of the vdP network dynamics on the grid (c), for the same corner-localized initial conditions as in (b). This circuit self-organizes into a stable active state in which edges and corners oscillate while the bulk synchronizes in-phase. (e,f) Snapshot of the vdP network dynamics on the grid (c) with edge (e) and bulk (f) defects. The vdP oscillator network remains polarized in the bulk, while active topological modes wrap around the defect. Simulation parameters: $\varepsilon = 0.1, g = 1, w = 5 \times 10^{-6}, s = g/2 - w$. Initial conditions: $x_1(0) = 2$ and $\dot{x}_1(0) = \dot{x}_j(0) = 0$ for $j \geq 2$.

by the linearized theory above [Fig. 2(c)]. Based on these observations, one expects that low-energy attractors with in-phase bulk dimer dynamics will also be dominant in more complex ATCs, and that their bulk and edge frequencies can be estimated from spectra of the coupling matrix β in the weak coupling limit.

ATC implementations become particularly powerful in $d \geq 2$ dimensions. Different types of 2D SSH lattices can be constructed by stacking 1D SSH chains and connecting them using alternating strong and weak couplings (Fig. 3). This procedure allows the realization of two essentially different topological regimes: T1 – only the edges along one of the coordinate axes are in the topological coupling regime [Fig. 3(a,b)]; T2 – all the edges are in the topological coupling regime [Fig. 3(c-f)] (Supplementary Information). In the T1-regime, topologically protected modes exist along two opposite edges of a finite sample [Fig. 3(b)], whereas in the T2-regime they exist only at the corners [22]. Because essential aspects of the dynamics are qualitatively similar for both cases, we focus our discussion on the T2-regime [Fig. 3(c)]. In this case, one can distinguish three different groups of oscillators: corner oscillators that are only weakly coupled to their neighbors, strongly coupled vdP dimers along the edges that are similar to the 1D case, and quartets of strongly coupled vdP oscillators in the bulk. Each quartet is weakly coupled to its neighbors or the boundary. Analogous to the 1D case, the linear stability of the quartets can be analyzed independently in the weak-coupling limit $w \rightarrow 0$. Then, the lowest-frequency mode is an in-phase state $(1, 1; 1, 1)$ with period $2\pi/\sqrt{g-2s}$ (Supplementary Information). Similar to the 1D case, in the limit $(g-2s) \rightarrow 0^+$, the bulk quartets collectively synchronize to the low-frequency in-phase state. However,

the dimers on the boundary now oscillate at a frequency lower than that of the corner nodes, because $(g-s) \rightarrow s$ as $(g-2s) \rightarrow 0^+$. This opens the intriguing possibility of using topological protected modes to precisely control active oscillations in 2D ATCs.

Initializing the 2D active SSH circuits with a nonzero voltage at one of the corner nodes, one finds that essential qualitative features of the dynamics seen in 1D ATCs carry over to the 2D case. In particular, the boundary nodes belonging to topologically protected corner modes as well as the non-protected edge nodes become activated one after the other and settle down in their respective vdP limit cycles. Similarly, in the bulk, quartets of strongly coupled oscillators synchronize. Because the in-phase state is the lowest-energy attractor above the quiescent state, the bulk synchronizes in a global in-phase pattern [Fig. 3(b,d)]. Thus, in both 1D and 2D ATCs, topologically protected edge modes become activated via self-sustained oscillations, while the bulk dynamics is almost decoupled, leading to synchronization.

Crucially, this ATC self-organization principle remains valid in the presence of defects, demonstrating that topological protection phenomena can survive in the nonlinear regime $\varepsilon > 0$ [Fig. 3(e,f)]. Introducing a boundary defect in a passive ($\varepsilon = 0$) 2D SSH grid by removing a few unit cells does not affect the localized nature of the edge state, which now wraps around the defect due to topological protection from the linear coupling. Self-sustained oscillations in nonlinear active ($\varepsilon > 0$) circuits inherit this topological protection globally: in the presence of edge defects, all boundary nodes continue to oscillate at a high non-zero frequency while bulk quartets synchronize at low frequency [Fig. 3(e)]. Similarly, bulk defects also lead to localized nonlinear edge oscillations [Fig. 3(f)].

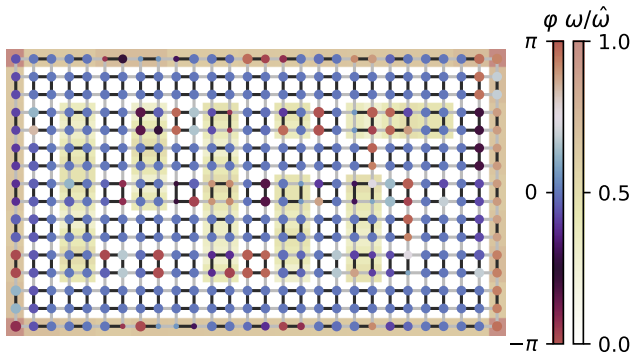


FIG. 4. Control of active traveling wave patterns through bulk defects. Activated in a single corner, the circuit self-organizes into a pre-programmed wave pattern. Simulation parameters: $\varepsilon = 0.5$, $g = 1$, $w = 5 \times 10^{-6}$, $s = g/2 - w$. Initial conditions: $x_1(0) = 2$ and $\dot{x}_1(0) = x_j(0) = \dot{x}_j(0) = 0$ for $j \geq 2$.

These results show that the SSH network topology can be used to precisely control the individual and collective behavior of coupled nonlinear oscillators.

Last but not least, the above ideas can be extended to achieve control of active traveling wave patterns by means of non-topological defects. By strategically placing bulk defects, one can guide the self-organization of active wave patterns that can be initiated from a single corner node (Fig. 4).

In conclusion, the theory of active topoelectrical circuits developed here promises a wide range of applications, from active wave guides to autonomous electronic circuits with topologically protected functionalities. The above framework can be integrated with recently developed methods for the inverse design of network-based metamaterial structures [50, 51], to optimize and tailor the node couplings and transmission properties. By designing the coupling matrix β such that the associated dynamical matrix possesses chiral [41] or other symmetries, it is possible to realize different topological phases with the vdP oscillator as a generic nonlinearity. Another intriguing prospect is the possibility of creating and studying electronic metamaterials with effective dimensions $d > 3$ that appear to be difficult to access otherwise. Beyond man-made devices, the above results suggest that it would be interesting to explore whether active biological circuits may use topological coupling regimes to facilitate robust signal transport and information storage.

This work was supported by a James S. McDonnell Foundation Complex Systems Scholar Award (J.D.) and the MIT Solomon Buchsbaum Research Fund (J.D.).

[1] R. FitzHugh, *Bull. Math. Biophysics* **17**, 257 (1955).

- [2] J. Nagumo, S. Arimoto, and S. Yoshizawa, *Proc. IRE* **50**, 2061 (1962).
- [3] E. Izhikevich, *Dynamical Systems in Neuroscience*, Computational neuroscience Dynamical systems in neuroscience (MIT Press, 2007).
- [4] V. A. Makarov, E. del Río, W. Ebeling, and M. G. Velarde, *Phys. Rev. E* **64**, 036601 (2001).
- [5] E. del Río, V. A. Makarov, M. G. Velarde, and W. Ebeling, *Phys. Rev. E* **67**, 056208 (2003).
- [6] S. Weimann, M. Kremer, Y. Plotnik, Y. Lumer, S. Nolte, K. G. Makris, M. Segev, M. C. Rechtsman, and A. Szameit, *Nat. Mater.* **16**, 433 (2017).
- [7] A. B. Khanikaev, S. Hossein Mousavi, W.-K. Tse, M. Kargarian, A. H. MacDonald, and G. Shvets, *Nat. Mater.* **12**, 233 (2013).
- [8] Y. Lumer, Y. Plotnik, M. C. Rechtsman, and M. Segev, *Phys. Rev. Lett.* **111**, 1 (2013).
- [9] Z. Yang, F. Gao, X. Shi, X. Lin, Z. Gao, Y. Chong, and B. Zhang, *Phys. Rev. Lett.* **114**, 114301 (2015).
- [10] C. Kane and T. Lubensky, *Nat. Phys.* **10**, 39 (2014).
- [11] S. D. Huber, *Nat. Phys.* **12**, 621 (2016).
- [12] L. M. Nash, D. Kleckner, A. Read, V. Vitelli, A. M. Turner, and W. T. Irvine, *Proc. Natl. Acad. Sci. U.S.A.* **112**, 14495 (2015).
- [13] B. G.-g. Chen, N. Upadhyaya, and V. Vitelli, *Proc. Natl. Acad. Sci. U.S.A.* **111**, 13004 (2014).
- [14] M. Z. Hasan and C. L. Kane, *Rev. Mod. Phys.* **82**, 3045 (2010).
- [15] B. A. Bernevig, T. L. Hughes, and S.-C. Zhang, *Science* **314**, 1757 (2006).
- [16] L. Fu, C. L. Kane, and E. J. Mele, *Phys. Rev. Lett.* **98**, 106803 (2007).
- [17] D. Hsieh, D. Qian, L. Wray, Y. Xia, Y. S. Hor, R. J. Cava, and M. Z. Hasan, *Nature* **452**, 970 (2008).
- [18] J. E. Moore and L. Balents, *Phys. Rev. B* **75**, 121306 (2007).
- [19] X. Qi and S.-C. Zhang, *Rev. Mod. Phys.* **83**, 1057 (2011).
- [20] A. Souslov, B. C. van Zuijden, D. Bartolo, and V. Vitelli, *Nat. Phys.* **13**, 1091 (2017).
- [21] F. G. Woodhouse, H. Ronellenfitsch, and J. Dunkel, *Phys. Rev. Lett.* **121**, 178001 (2018).
- [22] S. Imhof, C. Berger, F. Bayer, J. Brehm, L. W. Molenkamp, T. Kiessling, F. Schindler, C. H. Lee, M. Greiter, T. Neupert, and R. Thomale, *Nat. Phys.* **14**, 925 (2018).
- [23] C. H. Lee, S. Imhof, C. Berger, F. Bayer, J. Brehm, L. W. Molenkamp, T. Kiessling, and R. Thomale, *Nat. Commun.* **1**, 39 (2018).
- [24] J. Ningyuan, C. Owens, A. Sommer, D. Schuster, and J. Simon, *Phys. Rev. X* **5**, 021031 (2015).
- [25] V. V. Albert, L. I. Glazman, and L. Jiang, *Phys. Rev. Lett.* **114**, 173902 (2015).
- [26] K. Luo, R. Yu, and H. Weng, *Research* **2018**, 6793752 (2018).
- [27] Y. Hadad, J. C. Soric, A. B. Khanikaev, and A. Alù, *Nat. Electron.* **1**, 178 (2018).
- [28] M. Serra-Garcia, R. Süsstrunk, and S. D. Huber, *Phys. Rev. B* **99**, 020304 (2019).
- [29] K. Luo, J. Feng, Y. X. Zhao, and R. Yu, *arXiv preprint*, **11** (2018), arXiv:1810.09231.
- [30] X. Zhou, Y. Wang, D. Leykam, and Y. D. Chong, *New J. Phys.* **19**, 095002 (2017).
- [31] A. N. Poddubny and D. A. Smirnova, *Phys. Rev. A* **98**, 013827 (2018).

- [32] D. Leykam and Y. D. Chong, *Phys. Rev. Lett.* **117**, 143901 (2016).
- [33] D. Dobrykh, A. Yulin, A. Slobozhanyuk, A. Poddubny, and Y. S. Kivshar, *arXiv preprint arXiv:1805.03760* (2018).
- [34] S. Malzard and H. Schomerus, *New J. Phys.* **20**, 063044 (2018).
- [35] Y. Wang, L.-J. Lang, C. H. Lee, B. Zhang, and Y. Chong, *Nat. Commun.* **10**, 1102 (2019).
- [36] S. Sayed, S. Hong, and S. Datta, *Phys. Rev. Applied* **10**, 054044 (2018).
- [37] T. Jiang, M. Xiao, W.-J. Chen, L. Yang, Y. Fang, W. Y. Tam, and C. Chan, *Nat. Commun.* **10**, 434 (2019).
- [38] A. K. Iyer and G. V. Eleftheriades, *Appl. Phys. Lett.* **92**, 261106 (2008).
- [39] A. Forrow, F. G. Woodhouse, and J. Dunkel, *Phys. Rev. Lett.* **119**, 028102 (2017).
- [40] F. G. Woodhouse, A. Forrow, J. B. Fawcett, and J. Dunkel, *Proc. Natl. Acad. Sci. U.S.A.* **113**, 8200 (2016).
- [41] T. Hofmann, T. Helbig, C. H. Lee, and R. Thomale, *arXiv preprint arXiv:1809.08687* (2018).
- [42] B. B. Johnson, S. V. Dhople, A. O. Hamadeh, and P. T. Krein, *IEEE Trans. Circuits Syst. I, Reg. Papers* **61**, 834 (2014).
- [43] I. Gottlieb, *Practical Oscillator Handbook* (Elsevier Science, 1997).
- [44] J. J. Stoker, *Nonlinear vibrations in mechanical and electrical systems*, Vol. 2 (Interscience Publishers New York, 1950).
- [45] P. Romanczuk, M. Bär, W. Ebeling, B. Lindner, and L. Schimansky-Geier, *Eur. Phys. J. Special Topics* **202**, 1 (2012).
- [46] W. Su, J. Schrieffer, and A. J. Heeger, *Phys. Rev. Lett.* **42**, 1698 (1979).
- [47] J. K. Asbóth, L. Oroszlány, and A. Pályi, *A short course on topological insulators* (Springer).
- [48] D. Storti and R. Rand, *Int. J. Non-linear Mechan.* **17**, 143 (1982).
- [49] S. Wirkus and R. Rand, *Nonlinear Dyn.* **30**, 205 (2002).
- [50] A. Forrow, F. G. Woodhouse, and J. Dunkel, *Phys. Rev. X* **8**, 041043 (2018).
- [51] H. Ronellenfitsch, N. Stoop, A. Forrow, and J. Dunkel, *arXiv preprint arXiv:1802.07214* (2018).